

<https://doi.org/10.1038/s43247-024-01886-7>

Global upper ocean dissolved oxygen budget for constraining the biological carbon pump

Check for updates

Ryohei Yamaguchi¹ ✉, Shinya Kouketsu^{1,2}, Naohiro Kosugi³ & Masao Ishii³

One mechanism by which the ocean uptakes carbon dioxide is through the biological carbon fixation and its subsequent transport to the deep ocean, a process known as the biological carbon pump. Although the importance of the biological pump in the global carbon cycle has long been recognized, its actual contribution remains uncertain. Here, we quantify the carbon export from the upper ocean via the biological carbon pump by revealing the upper ocean dissolved oxygen balance. Calculations of dissolved oxygen budget quantified net oxygen removals from the upper ocean by physical processes (air–sea exchange, advection, and diffusion) and indicated net biological oxygen production that compensated for those removals. The derived oxygen production is converted to carbon units using the photosynthetic ratio, and inferred an estimated global annual carbon export through the biological pump of 7.36 ± 2.12 Pg C year⁻¹ with providing insights into the overall ocean carbon cycle.

The ocean serves as a vast carbon reservoir in the Earth's carbon cycle¹ and plays a crucial role in regulating decadal to millennia-scale climate by absorbing and sequestering CO₂ and hence controlling atmospheric CO₂ concentration^{2,3}. Part of the CO₂ dissolved in the ocean becomes fixed as organic carbon through upper ocean net ecosystem productivity. Although most of the organic carbon formed is eventually respired back into inorganic carbon, organic matter transported away from the upper ocean (commonly referred to as “export flux/production”) contributes to long-term oceanic carbon storage. These processes are the so-called “biological carbon pump”, which is one of the important processes responsible for ocean CO₂ uptake. Recently, in addition to the gravitational settling of particulate organic carbon (POC) as the classical concept of the biological carbon pump, the transport of dissolved organic carbon^{4,5} (DOC) and the transport of DOC and POC by mesoscale eddies^{6–8} and sub-mesoscale structures⁹, as well as the transport associated with vertical movements of mesopelagic migrators¹⁰, are thought to contribute substantially to the export of organic carbon to the deep ocean¹¹, that is, to the biological carbon pump.

Global observational quantification of the carbon fixed and exported to the deep ocean through the biological pump remains insufficiently constrained^{12–14} due to a lack of direct observations that can be mapped globally and a lack of understanding of the processes that can be modeled. Various approaches have been used to provide global estimates, including estimates from satellite data^{15,16} and chemical tracer fields^{17,18}, extrapolation of in situ direct measurements¹⁹, combinations of observations and mechanical models^{20,21}, and data assimilation using ocean biogeochemical

models^{22,23}, yielding estimates ranging from 4 to 13 Pg C year⁻¹. This weak observational constraint stands in contrast to the relatively well-constrained global estimate of air–sea CO₂ exchange for the recent decade (2.8 ± 0.4 Pg C year⁻¹, mean \pm SD)²⁴, despite both being essential components of the global carbon cycle. This is partly because of the difference in the number of observations required to quantify them due to the different complexities among their underlying processes. The weakness of observational constraints complicates the validation of Earth system models (ESMs)²⁵, potentially introducing one of the causes of uncertainties in the future climate projections by ESMs.

With recent technical advancements in the measurement of dissolved oxygen concentrations by autonomous profiling floats²⁶, methodologies for indirect quantifying the biological carbon export from year-long dissolved oxygen data are also being developed and applied over spatially broader regions²⁷, beyond the traditional ocean stations. Autonomous profiling floats, such as the Biogeochemical-Argo (BGC-Argo) float, provide relatively high-frequency (more than once per month), long-term (~5–7 years), and spatially broader observations of the upper ocean dissolved oxygen²⁸. By subtracting dissolved oxygen changes induced by various physical processes from the observed oxygen time series, it is possible to obtain the net production of oxygen by biological processes. As the oceanic biological oxygen and organic carbon production are linked via the photosynthetic stoichiometry²⁹, the net biological oxygen production can be converted into the net organic carbon production (total production minus autotrophic and heterotrophic respiration), which is referred to as the net community

¹Research Institute for Global Change, Japan Agency for Marine–Earth Science and Technology, Yokosuka, Japan. ²Advanced Institute for Marine Ecosystem Change (WPI-AIMEC), Japan Agency for Marine–Earth Science and Technology, Yokohama, Japan. ³Meteorological Research Institute, Japan Meteorological Agency, Tsukuba, Japan. ✉e-mail: ryamaguchi@jamstec.go.jp

production (NCP). Under steady-state conditions (i.e., no net organic carbon accumulation) and with averages taken over a broader spatial extent in which lateral organic carbon exchanges become negligible, the upper ocean NCP is identical to the amount of organic carbon exported from the upper ocean into ocean interior. Recent expansion of the BGC-Argo network has led to a remarkable increase in the number of dissolved oxygen profiles obtained and improved spatial coverage. Consequently, estimates of NCP derived indirectly from float-based dissolved oxygen data have the potential to overcome the spatial limitations of previous estimates, and hence provide a more robust global constraint of the biological carbon pump.

To globally quantify the amount of organic carbon exported through the biological pump, we expanded previously established local framework for upper ocean dissolved oxygen budget^{30–32} to the global ocean, with explicitly incorporating lateral physical processes that could potentially play an important role in the global budget. An equation for the upper ocean dissolved oxygen budget indicates that upper ocean dissolved oxygen integrated vertically from sea surface to a depth (O_{2int}) varies because of fluxes due to physical processes, such as air–sea exchange (F_{A-S}), horizontal and vertical advection (F_{ADV}), horizontal diffusion (F_{hDIFF}) and vertical diffusion (F_{vDIFF}), as well as the net biological production (F_{NCP}):

$$\frac{\partial O_{2int}}{\partial t} = F_{A-S} + F_{vDIFF} + F_{ADV} + F_{hDIFF} + F_{NCP} \quad (1)$$

Integrating Eq. (1) over a climatological annual cycle, the left side tends to zero. Further spatial integration over the global ocean gives the global net biological oxygen production (NBP_{O_2}) as

$$NBP_{O_2} = - \int_{year} \int_{global} (F_{A-S} + F_{vDIFF} + F_{ADV} + F_{hDIFF}) dt dA. \quad (2)$$

This equation was applied to the climatological annual cycles computed from oxygen data from 1980 to 2022 for which the spatial data coverage becomes sufficient. We first estimated the four physical oxygen fluxes as their climatological monthly maps using multiple observational and reanalysis products and then determined the global annual net biological oxygen production using these maps. The annual net oxygen production obtained was then converted to annual net community production (ANCP) by using the photosynthetic quotient³³, $\Delta O_2/\Delta C = 1.45$ (see Methods for further details).

The biological carbon fixation primarily occurs in the sunlit upper ocean, known as the euphotic zone. The fixed organic carbon exported to layers below has the potential to contribute to the long-term ocean carbon sequestration. However, given the typical upper ocean situation that the annual maximum of the surface mixed layer depth (MLD) is deeper than that of the euphotic layer depth (Z_{eu}), with the exception of oligotrophic subtropical oceans (Fig. 1a, b), a considerable portion (~10–90%³⁴) of the organic carbon exported during the warm productive season can be re-

entrained into the mixed layer by the subsequent winter mixing. The re-entrained organic carbon can be respired back to the inorganic form and then utilized to production in the euphotic layer or exposed to the air–sea gas exchange again, thus is not able to contribute the long-term ocean carbon sequestration.

In this study, to quantify the organic carbon export that escapes such upper ocean seasonal cycle and reaches to deeper layers, we defined the depth of the lower boundary of the upper ocean used in the calculation of the dissolved oxygen budget (here referred to as depth H) as the deeper of the annual maximum MLD or the annual maximum Z_{eu} (Fig. 1c); therefore the resultant ANCPs represent the organic carbon fluxes crossing the H -plane over the course of one year with having more than one-year sequestration time-scale. As will be seen later in Results, it is noted that the ANCPs estimated in this study tend to be smaller than the traditional ANCPs defined in the euphotic layer, so we add a subscript H to distinguish the ANCPs in this study ($ANCP_H$) from the traditional definition.

Results

Upper ocean dissolved oxygen balance

At the sea surface, oxygen is exchanged between the atmosphere and the ocean (Fig. 2a). In the mid- to high latitudes, the air–sea oxygen exchanges exhibit pronounced seasonality. The strong air–sea oxygen gradient in the cold season is a consequence of undersaturated sea surface oxygen, which results from the rapid cooling and continuous supply of relatively low oxygen water from below due to the surface cooling and associated convection. It promotes net oxygen uptake during winter, whereas net outgassing is driven by reduced solubility due to surface heating and increases in dissolved oxygen due to enhanced biological production during warm periods. Much of the global ocean experiences a net loss of oxygen on an annual average basis due to air–sea exchange. Some regions, such as the eastern equatorial Pacific, the southern subtropical Indian Ocean, high latitudes of the North Atlantic and the Southern Ocean, exhibit an annual net oxygen uptake. In addition to the typical diffusive air–sea oxygen flux driven by the air–sea gradient of the concentrations and the surface winds, air–sea oxygen exchange mediated by bubbles also contributes to the high-latitude net uptake (Supplementary Fig. 1). Globally integrated, 206 ± 246 Tmol O_2 (mean \pm estimated error; see Methods for uncertainty estimation) is being removed annually from the ocean, consistent with the sign inferred from global ocean deoxygenation^{35–37}. Previous estimates derived from the bulk relationship between global ocean oxygen and heat content during the same period of analysis^{38–42} fall within the range of uncertainty range of our estimate.

At the lower boundary of the upper ocean (depth H), the vertical diffusion fluxes serve to reduce oxygen annually from the upper ocean over an entire region, as dissolved oxygen concentrations generally increase closer to the air–sea interface (Fig. 2b). The spatial distribution is more indicative of the spatial distribution of vertical oxygen gradient intensities at depth H , rather than of the vertical diffusion coefficient used

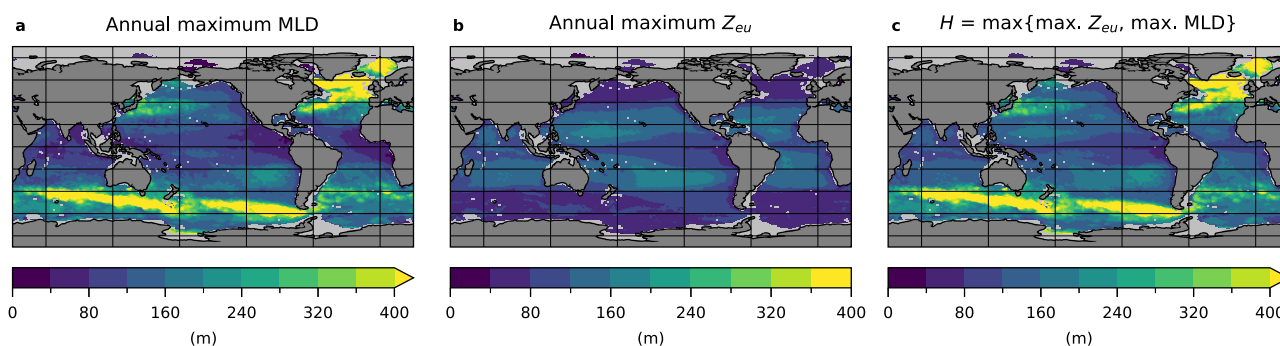


Fig. 1 | Distribution of the water surface used to set the lower boundary of the upper ocean dissolved oxygen budget. a Annual maximum mixed layer depth⁷³ (MLD). **b** Annual maximum euphotic layer depth⁷⁴ (Z_{eu}). **c** Defined surface for the

lower boundary of the upper ocean dissolved oxygen budget calculation (depth H) as the deeper of the annual maximum of MLD and that of Z_{eu} .

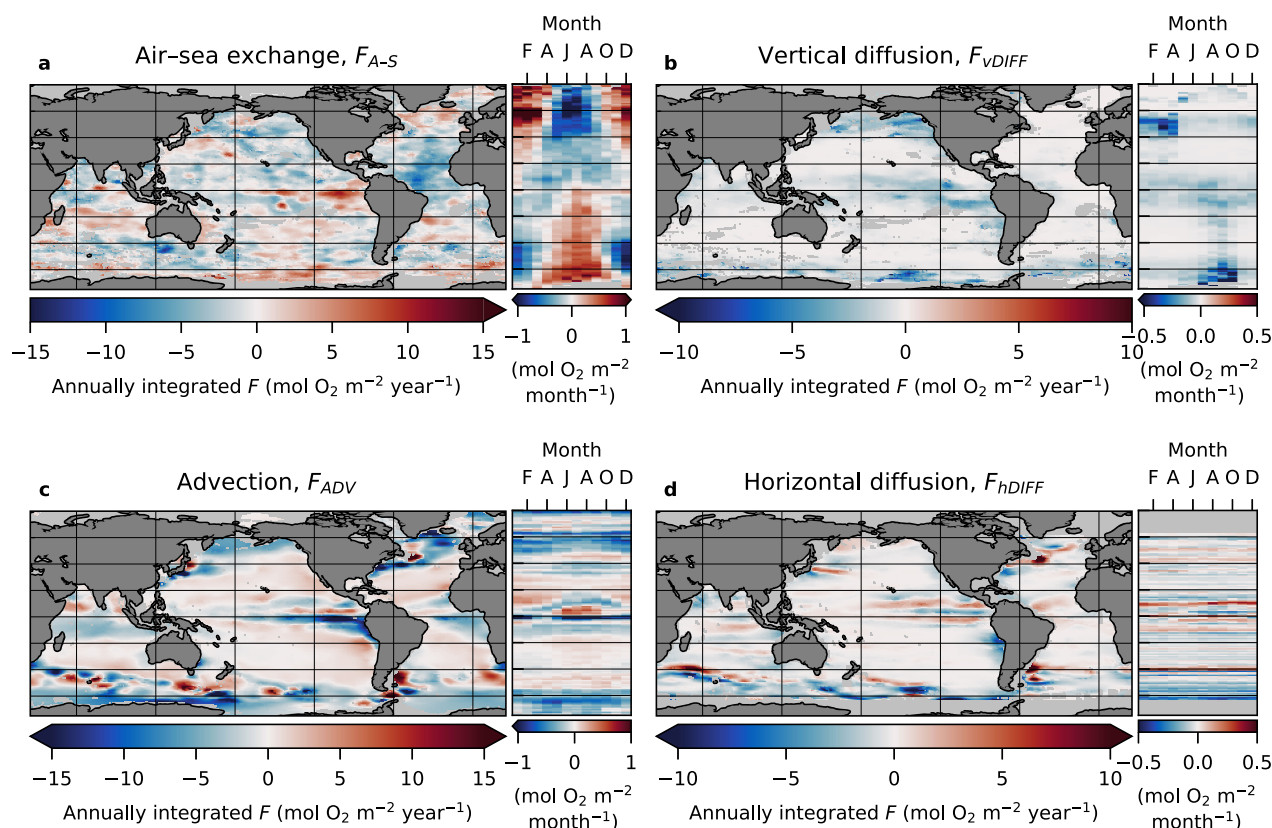


Fig. 2 | Annually integrated physical oxygen fluxes that contribute to the upper ocean dissolved oxygen balance. Spatial patterns of four annually integrated physical oxygen fluxes (left side of each panel) and their zonal mean seasonal cycles (right side of each panel). **a** Air-sea oxygen exchange (F_{A-S}); **b** vertical diffusion of oxygen ($F_{V,DIFF}$) at the lower boundary (depth H); **c** advection of oxygen (F_{ADV}); and

d horizontal diffusion of oxygen ($F_{H,DIFF}$). A negative flux indicates oxygen removal from the upper ocean. Note that the maps of the advection term (**c**) and the horizontal diffusion term (**d**) are spatially smoothed to match the horizontal mapping scale of the air-sea exchange and vertical diffusion term.

(Supplementary Fig. 2). Pronounced downward fluxes occur in regions with strong vertical oxygen gradients, such as the subarctic North Pacific and the eastern equatorial Pacific. In regions where H is defined as the annual maximum MLD, such as in mid- to high latitudes (c.f., Fig. 1), winter diffusion fluxes tend to be stronger because the base of the winter mixed layer, i.e. strong diffusivity layer, is closer to the temporally fixed depth H .

Physical processes other than air-sea exchange and vertical diffusion also play a crucial role in the global upper ocean dissolved oxygen balance⁴³. The advection fluxes result in an annual net removal of upper ocean oxygen, especially in regions of wind-driven upwelling (e.g., the eastern equatorial Pacific and Atlantic, and the Southern Ocean) and water-mass obduction⁴⁴ (e.g., subarctic/subpolar gyres), as low-oxygen water from deeper layers moves above depth H (Fig. 2c). The horizontal diffusion fluxes exhibit higher values along regions characterized by strong currents (Fig. 2d). On a global scale, physical oxygen fluxes from vertical diffusion, advection, and horizontal diffusion, annually remove 248 ± 33 , 316 ± 38 , and 120 ± 49 Tmol O₂ from the upper ocean, respectively.

The sum of these annual physical oxygen fluxes should balance the net annual biological oxygen production (equation [2]) under the assumption of the steady-state condition (Fig. 3). The global annual net biological oxygen production is estimated to be 889 ± 256 Tmol O₂ year⁻¹. Using the $\Delta O_2 : \Delta C$ ratio³³ of 1.45 ± 0.03 , the climatological global ANCP_H over the analysis period (1980–2022) can be estimated as 7.36 ± 2.12 Pg C year⁻¹. Given the definition of depth H in this study, this result implies that, globally, through the biological pump, the equivalent amount of carbon, in either particulate or dissolved form, escapes from the predominant upper-ocean seasonal cycle of physical environmental conditions (e.g., mixing and restratification) and becomes sequestered into the ocean interior on longer timescales than, at shortest, one year.

Note that, during the derivation of Eq. (2), we made the assumption of a steady state in terms of the total amount of the upper ocean dissolved oxygen over the four decades of the analysis period, although the current state of ocean deoxygenation is an undeniable fact supported by evidence from multiple observations^{35–37}. However, considering that a previous estimate³⁷ of deoxygenation in the upper 200 m was approximately 10 Tmol O₂ year⁻¹ (c.f., global mean $H = 186$ m), the potential error from our assumption is smaller than the uncertainties from other sources of error, and hence its impact is considered minor in this budget calculation.

Global ocean ANCP based on dissolved oxygen budget

The estimated ANCP_{HS}, which have a global mean of 1.7 ± 0.5 mol C m⁻² year⁻¹, exhibit a characteristic latitudinal variation, with substantial zonal variations over each ocean basin (Figs. 4a and 4f). The average ANCP_H in the Northern Hemisphere (NH, 2.0 mol C m⁻² year⁻¹) is larger than that in the Southern Hemisphere (SH, 1.5 mol C m⁻² year⁻¹), implying hemispheric differences in vertical and lateral supplies of nutrients and atmospheric deposition that support productions. The result indicates that, considering the area of ocean in each hemisphere, almost the same amount of carbon is fixed and exported into the ocean interior through the biological pump.

Each ocean basin shares the meridional variation in ANCP_{HS}, with relatively high ANCP_{HS} in the high latitudes and equatorial regions and lower values in the subtropics (Fig. 4c, d). On the other hand, it indicates considerable differences in the average ANCP_{HS}: 1.1 mol C m⁻² year⁻¹ in the Indian Ocean, 1.6 mol C m⁻² year⁻¹ in the Pacific Ocean, and 1.9 mol C m⁻² year⁻¹ in the Atlantic Ocean. A previous study⁴⁵ has identified the similar contrast among basins, which is likely attributable to difference in nutrient supply from the Southern Ocean⁴⁵ and/or low-latitude mesopelagic nutrient

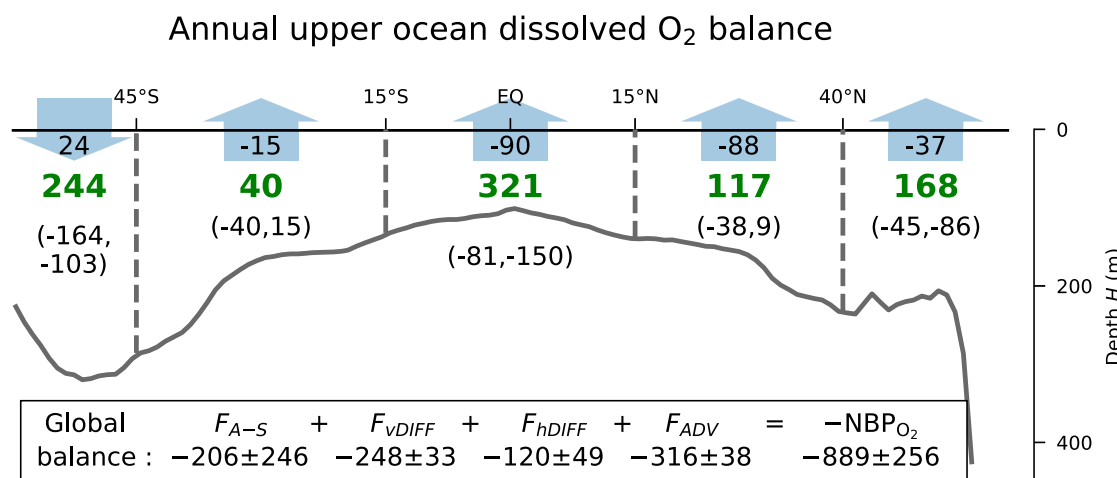


Fig. 3 | Annual upper ocean dissolved oxygen balance. Zonally integrated upper ocean dissolved oxygen balance for five latitudinal bands, including physical oxygen transfers by air–sea exchange (F_{A-S} , the top numbers with arrows), diffusion ($F_{vDIFF} + F_{hDIFF}$, the first numbers in parentheses), and advection (F_{ADV} , the second

numbers in parentheses), and net biological production of oxygen (F_{NCP} , green bold numbers). The black line shows the zonal mean depth H . Global balance (Eq. (2)) is reported as the sums with their uncertainties in the bottom box (see Methods for uncertainty estimation). The unit of all budget terms are $Tmol\ O_2\ year^{-1}$.

recycling⁴⁶. Our method in which the dissolved oxygen budget is calculated should result in spatial patterns of $ANCP_{HS}$ that reflect the sum of the terms in the physical oxygen fluxes (Fig. 4b). The results highlight that the physical processes such as advection and diffusion play a crucial role in closing the upper ocean dissolved oxygen budget at not only global scale but also regional scale, particularly in high latitudes and equatorial regions.

The obtained $ANCP_{HS}$ with their zonal variabilities show good overall agreement with previous local estimates (Fig. 4c–f). In general, the result of estimating $ANCP_H$ from tracer budgets highly depends on the definition of H (i.e., the depth at which the export is estimated). The $ANCP_{HS}$ in this study are derived from the net biological oxygen production, i.e., biological production minus autotrophic/heterotrophic respirations. Since the biological production dominates in the euphotic layer, and as it goes deeper, respirations become relatively dominant, the deeper the depth H , the smaller the $ANCPs$ tend to be⁴⁷. As this study uses a deeper H compared to the previous float-based and ocean station studies, which used the seasonally varying MLD⁴⁸ or Z_{eu} ⁴⁹, or fixed depths of 100 m or 200 m^{50,51}, $ANCP_{HS}$ from this study could reflect a greater influence from subsurface respiration, leading to lower $ANCPs$. Furthermore, using a skin temperature correction⁵² when calculating air–sea oxygen exchanges could also be one of the reasons why our $ANCP_{HS}$ are on the smaller side (see also Supplementary Note 3 for further details).

In addition to such discrepancies with a part of previous estimates due to the difference in the definition for calculations, potential biases arising from limitations of data used in this study also warrant attention. Direct carbon export by meso-scale eddies and associated submeso-scale structures, known as the Eddy-pump, is believed to account for ~20% of the total in the eddy-rich Southern Ocean⁸. Although the bolus velocities from a reanalysis product were used in our budget calculations, the eddy transport of oxygen (F_{ADV}^* in Fig. 4b) computed from the parameterized eddy transport and the spatially smoothed dissolved oxygen fields might be underestimated. And, in the air–sea oxygen flux calculations, we used raw profile values to calculate instantaneous oxygen flux, which are then smoothed into monthly temporal resolutions in the subsequent spatial mapping. This could lead to underestimations of episodic and intense biogenic oxygen releases that could occur on relatively short time scales. Both aspects require further verification through additional observational studies as more data is accumulated.

Local perspective for dissolved oxygen balance and NCP

Even within the same ocean basin, the seasonal upper ocean dissolved oxygen balances are distinct among the subtropics (near the Hawaii Ocean

Time-series station, HOT), the region associated with the western boundary current (Kuroshio-Oyashio Confluence Region, KOOCR), and the subarctic (near the Ocean Station P, OSP), which were selected as regions with an abundance of observations (c.f., Supplementary Figs. 3 and 4).

In the subtropics, situated far from strong currents, the oxygen tendency in the budget is primarily determined by the balance between air–sea exchange (F_{A-S}) and net biological production (F_{NCP}) (Fig. 5a). The NCP remains positive throughout the most of the year, resulting in a carbon export of about $1\ mol\ C\ m^{-2}\ year^{-1}$ into the dark ocean annually through the biological pump. In the KOOCR, oxygen reduction by advection (F_{ADV}) due to the obduction⁵³ of low-oxygen water mass from the layer below the depth H also plays an important role in the upper ocean dissolved oxygen balance⁵⁴ (Fig. 5c). Although there is a substantial seasonal amplitude of vertically integrated oxygen, the resultant $ANCP_H$ remains modest. In the eastern subarctic (OSP), the remarkably strong vertical oxygen gradient around the winter MLD makes vertical diffusion an important factor in oxygen reduction during the winter (Fig. 5e). The resulting seasonal cycle of NCP at OSP is more consistent with a previous case study that explicitly accounted for lateral physical oxygen fluxes⁵⁵.

The relationship between the annual maximum MLD and Z_{eu} reflects the processes that regulate the seasonal cycle of physical environments. In the region near HOT, where the annual maximum Z_{eu} is deeper than the annual maximum MLD, positive NCPs are maintained by the strong production after spring, as suggested from the increase in dissolved oxygen (decrease in apparent oxygen utilization [AOU]) around the lower part of the mixed layer (Fig. 5b). On the other hand, in the KOOCR, where the annual maximum MLD is substantially deeper than the annual maximum Z_{eu} , the vertically integrated NCP becomes negative (i.e., respiration exceeds production) even during what is generally the productive period (spring to summer). This can be attributed to intense subsurface respiration during the productive periods in the thick layer below the Z_{eu} but above H , which is implied from the strong AOU increases within this layer from April to September (Fig. 5d). This demonstrates that the upper ocean condition of the physical environments (here, the resultant relationship between MLD and Z_{eu}) is one of the important controlling factors for determine the local carbon export. And, because of the considerable seasonality of subsurface respiration, estimates of $ANCP$ derived from mesopelagic oxygen changes during the productive season only^{51,56,57} must be interpolated with caution.

Discussion

The $ANCP_{HS}$ estimated from oxygen differs in principal from those inferred from satellite data, allowing for an independent comparison with satellite-

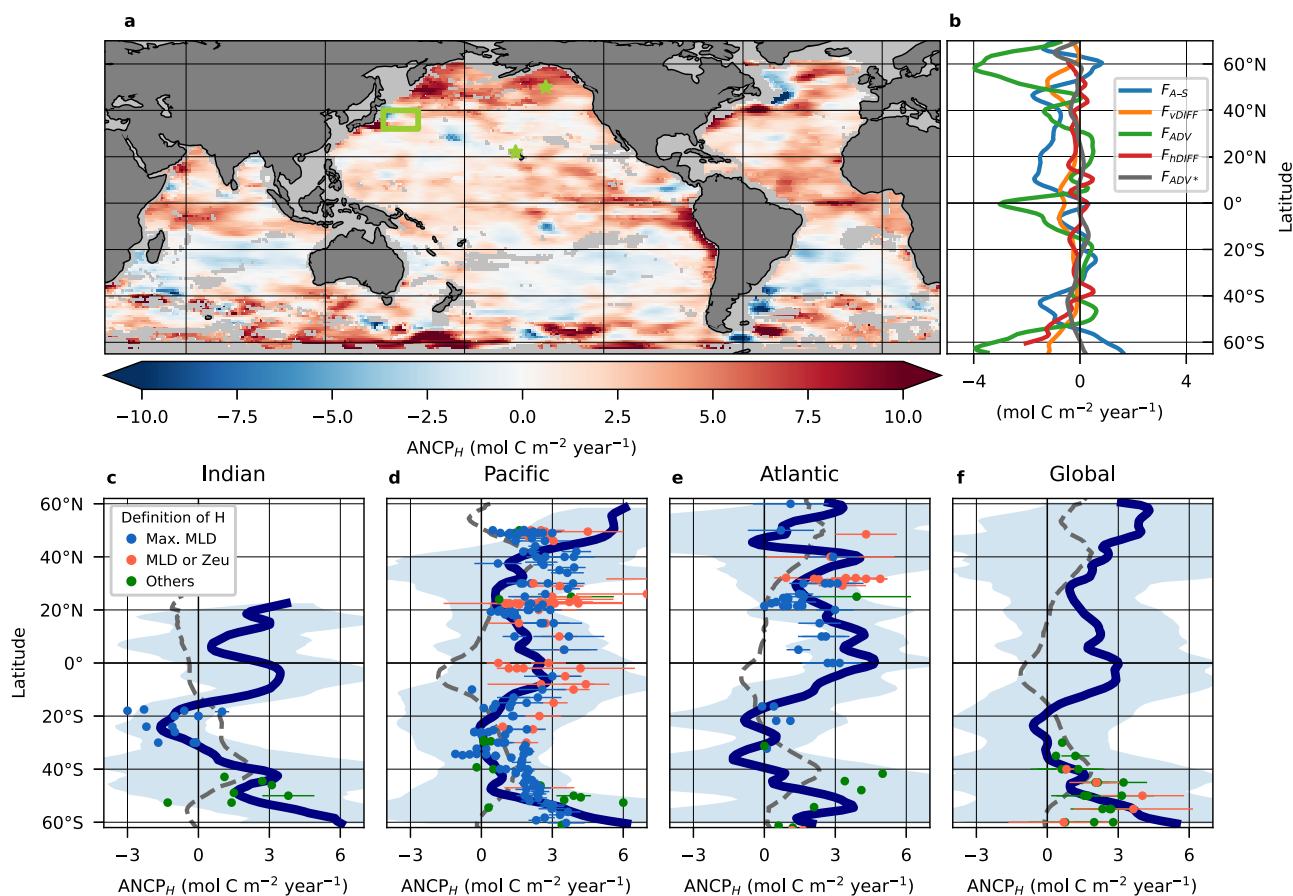


Fig. 4 | Global O₂-based annual net community production (ANCP). **a** Spatial pattern of ANCP (positive values indicate net production) obtained from the sum of four oxygen fluxes due to physical processes. Green boxes and stars indicate the region defined as the Kuroshio-Oyashio Confluence Region (KOCR), and the locations of the Hawaii Ocean Time-series (HOT) and the Ocean Station P (OSP). **b** Zonal means of the four physical oxygen fluxes and the bolus component of oxygen advection (F_{ADV^*}). The units were converted to carbon units with a $\Delta O_2:\Delta C$ ratio of 1.45. **c–f** Zonal mean O₂-based ANCP estimated in this study (blue lines) and previous local estimates (blue, orange, and green dots). The dots' colors represent the definition of the depth defined as the lower boundary of the upper ocean when

determining the ANCP (depth H in case of this study); annual maximum MLD (blue), seasonally varying MLD or Z_{eu} (orange), and the others (green). The horizontal lines accompanied by dots indicate their uncertainties where these are available (all data and their references are summarized in Supplementary Table 1). Blue shading indicates a range of two standard deviation of the zonal mean. The dash line in **c–f** shows the zonal mean climatological (1985–2018 mean) surface CO₂ flux from an observation-based global monthly gridded products⁸⁸ submitted to the ocean branch of phase two of the REgional Carbon Cycle Assessment and Processes (RECCAP2-ocean) project.

derived net primary production (NPP^{58–60}). The latitudinal trends of both ANCP_H and ANPP exhibit a decrease from the equator northward followed by an increase, showing a coherent pattern in the NH (Figs. 4f and 6). In the SH, ANCP_Hs increase southwards after reaching their minimum at 30°S, but ANPPs show the minimum values at the southern end of this analysis (60°S). Dividing the obtained zonal mean ANCP_H by the satellite-derived ANPP yields the export ratio, under the assumption of the annual steady state for the zonal-mean (i.e., ANCP_H can be considered equivalent to the annual export production). The ratios indicate a relatively stable latitudinal variation in the NH, with slightly higher values at high latitudes (Fig. 6). On the other hand, in the SH, reflecting the different behaviors among ANCP_H and ANPP, there is a marked latitudinal variation, with very low ratios in the subtropics and high ratios reaching up to 75% in the Southern Ocean. The previous parameterizations^{15,61} capture the latitudinal features of the export ratio in the NH but not in the SH. Given the latest global NPP estimate⁶² of 53 Pg C year⁻¹, the global export ratio becomes 0.14.

Combined with the air–sea inorganic carbon (CO₂) fluxes, the present-day long-term mean distribution of biological-driven organic carbon export presented in this study implies a comprehensive view of the overall of upper ocean carbon cycle (Fig. 4c–f). In the Pacific (Fig. 4d), as is largely common across other ocean basins, the amount of carbon exported from the upper ocean by the biological pump exceeds the inorganic carbon supplied from

the sea surface in the high latitudes. This divergence of carbon fluxes requires the net upward (and/or horizontal) physical supplies of inorganic carbon into the upper ocean supporting the substantial biological production, suggesting the dominant role of the biological pump in the ocean carbon pumps. On the other hand, in the subtropics of both hemispheres, more inorganic carbon is supplied by the air–sea flux than the amount of organic carbon exported from the upper ocean. This upper ocean convergence of carbon fluxes in subtropics indicates the anthropogenic accumulation of the inorganic carbon within the upper ocean and/or the net removal of inorganic carbon from the upper ocean due to the vertical/horizontal physical transport. Therefore, in this region, both physical and biological pumps contribute to the carbon export from the upper ocean. In tropical regions, the upper ocean carbon appears to be diverging due to strong surface CO₂ release and biological-driven export. This divergence can be balanced by the physical supply of inorganic carbon from the depths due to equatorial upwelling, emphasizing again the important role of the biological pump in transporting carbon to deeper layers in the tropics. These global perspective of the upper ocean carbon cycle described here from the observational tracer budget support the results from a previous model study⁶³.

Considering the sequestration time-scale of one year, our estimation of the global carbon export is consistent with the latest independent estimate

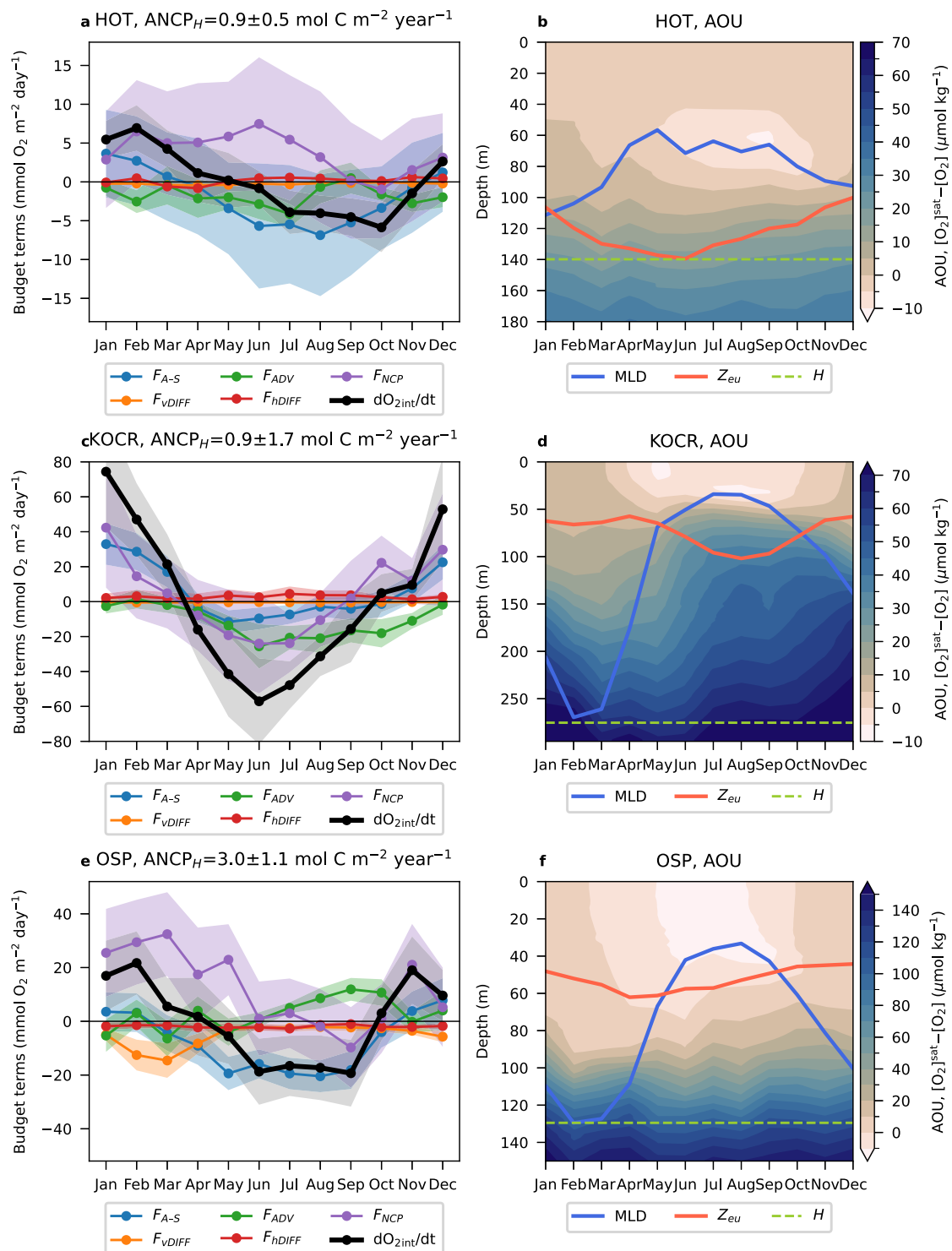


Fig. 5 | Local upper ocean dissolved oxygen budgets and apparent oxygen utilization (AOU). a, c, e Monthly upper ocean dissolved oxygen budgets (Eq. (1)) near the Hawaii Ocean Time-series (HOT) station, the Kuroshio-Oyashio confluence region (KOOCR), and the Ocean Station P (OSP), respectively. Shading along the lines indicates the uncertainties (see Methods for uncertainty estimation).

b, d, f Seasonal cycles of the apparent oxygen utilization (AOU, [O₂]^{sat} - [O₂]) at the same locations. Blue, red, and green lines indicate the surface mixed layer depth (MLD), euphotic layer depth (Z_{eu}), and the lower boundary of the upper ocean as defined in this study (depth H), respectively.

obtained through an inversion⁶⁴, falling within their range of uncertainties. We believe that our results could contribute to the observational constraints of the global biological pump. Although there are still some difficulties to be improved, such as uncertainties in the conversion of oxygen to carbon etc., the dissolved oxygen budget methodology has the great advantage of incorporating the results of most of diverse downward pathways of

biological carbon pump which make the direct field measurement difficult. With further improvement in the spatiotemporal coverage of the data, the methodology that has been developed over nearly half a century^{65,66} has the potential to enable us to monitor inter annual, decadal or longer time-scale changes in the biological carbon export and to help us understand their roles on the changing climate.

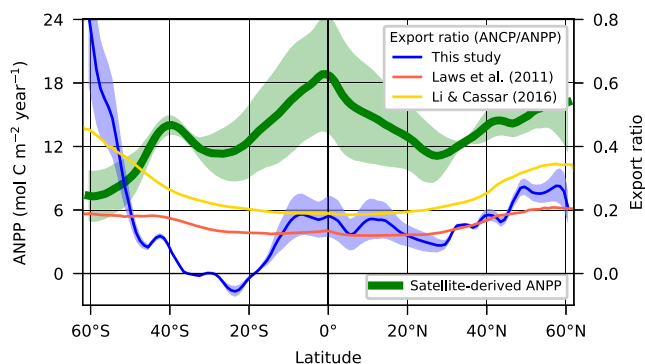


Fig. 6 | Latitudinal trend in the export ratio derived from the O₂-based ANCP. Satellite-derived annual net primary production (ANPP; green line, left y-axis) and the export ratios (ANCP/ANPP, right y-axis) computed using the O₂-based ANCP estimated in this study (blue line) and based on two empirical parametrizations (red¹⁵ and yellow⁶¹ lines). Shading around the lines indicates a range of one standard deviation among the three satellite-derived NPP products: vertically generalized production model (VGPM)⁵⁸; carbon-based production model (CbPM)⁵⁹; and carbon, absorption, and fluorescence euphotic-resolving (CAFE) model⁶⁰. The export ratio following Laws et al. (2001) is calculated by their equation (2) (ef-ratio) with using the three products mean of ANPP and a sea surface temperature climatology⁹². The export ratio following Li and Cassar (2016) is calculated by their equation (7) with using a sea surface temperature climatology⁹².

Because of international efforts to develop and maintain a network of global observations, we are at the beginning of an era where the export production through the biological pump can be globally estimated from in situ observed data, without relying on conventional remote sensing data. The accumulation of multiple independent descriptions using various different tracers can facilitate a more comprehensive understanding of the biological processes themselves that drive the biological pump by revealing more detailed vertical structure and seasonal development beyond the vertically integrated and annual mean basis of this study. The ability to estimate the horizontal and vertical distribution of dissolved substances and their budget on nearly global spatial coverage from observational data must contribute to a more detailed three-dimensional picture of the ocean carbon cycle and should be useful for validation of ESMs. International collaboration to maintain these observations is indispensable for updating our knowledge and refining ocean biogeochemical models and then for understating ongoing and forthcoming global changes.

Methods

Dissolved oxygen data

In this study, we used dissolved oxygen profiles observed from 1980 to 2022, sourced from the World Ocean Database (WOD) 2018⁶⁷, the BGC-Argo data from the Argo Global Data Assembly Centre⁶⁸, and the Global Ocean Data Analysis Project (GLODAP) version 2.2022⁶⁹ (Supplementary Figs. 3 and 4). From the WOD, profiles obtained by ship-base observations (datasets named as “OSD” and “CTD”) were used. We checked for duplicate observations by research cruises among the GLODAP and WOD based on the dates and locations of the observations, and prioritized them for use in the order GLODAP and WOD. Only dissolved oxygen values classified as “good” by the Quality Control (QC) procedure for each database were used: “Data mode = Adjusted or Delayed” and “Profile QC Flag = A or B” for BGC-Argo data⁷⁰, and “QC flag = 0” for WOD data⁶⁷. Furthermore, for analyses that require not only sea surface values but also vertical profiles, we excluded profiles where the shallowest oxygen observation layer was deeper than 15 m, profiles where the spacing of vertical observation layers was wider than 50 m above 150-m depth or wider than 100 m above the 400-m depth, and profiles with fewer than eight observations above 200-m depth (Supplementary Fig. 4). For profiles from autonomous profiling floats, we corrected biases at the base of the mixed layer due to the slow response time

of the dissolved oxygen sensor following the method proposed by a previous study³¹.

To calculate the horizontal gradients of dissolved oxygen required for estimating physical oxygen fluxes through advection and horizontal diffusion (Methods “Calculation of physical oxygen fluxes”), we also used two global ocean dissolved oxygen gridded products, the World Ocean Atlas 2018⁷¹ (WOA 2018) and Gridded Ocean Biogeochemistry from Artificial Intelligence-Oxygen⁷² (GOBAI-O₂). Both products are based on observational data: WOA 2018 provides optimally interpolated monthly climatology of dissolved oxygen from profiles obtained by various observational platforms, including ships and autonomous profiling floats, which are archived in WOD 2018, and GOBAI-O₂ contains dissolved oxygen data from BGC-Argo floats spatially interpolated using machine learning techniques at 1° (latitude) × 1° (longitude) horizontal resolution and monthly temporal resolution.

Upper ocean dissolved oxygen budget

Neglecting the cross-boundary flux due to molecular diffusion, dissolved oxygen concentration ([O₂]) within a water parcel undergoes changes based on the difference between biological production and respiration (*J*, positive indicates net production),

$$\frac{D[O_2]}{Dt} = J. \tag{3}$$

Integrating Eq. (3) vertically from the surface (*z* = 0) to a depth (*z* = −*H*) and rewriting it yields an equation for the upper ocean dissolved oxygen budget:

$$\begin{aligned} \frac{\partial}{\partial t} \int_{-H}^0 [O_2] dz = & F_{A-S} - \kappa_v(-H) \left. \frac{\partial [O_2]}{\partial z} \right|_{z=-H} + \int_{-H}^0 \nabla_h \bullet \kappa_h \nabla_h [O_2] dz \\ & + \int_{-H}^0 -(\mathbf{v} + \mathbf{v}^*) \bullet \nabla [O_2] dz + \int_{-H}^0 J dz, \end{aligned} \tag{4}$$

where κ_v and κ_h are vertical and horizontal diffusion coefficients, and \mathbf{v} and \mathbf{v}^* represent current velocities and their bolus components, respectively (Supplementary Note 1 for the derivation).

According to Eq. (4) (equivalent to Eq. (1)), the vertically integrated dissolved oxygen concentration is subject to variations caused by air–sea exchange at sea surface (*F*_{A-S}), vertical diffusion at the depth *H* (*F*_{VDIFF}, the second term on the right side of Eq. (4)), horizontal diffusion (*F*_{HDIFF}, the third term on the right side of Eq. (4)), advection (*F*_{ADV}, the fourth term on the right side of Eq. (4)), and net biological production within the layer (*F*_{NCP}, the last term on the right side of Eq. (4)). In this study, we applied Eq. (4) to a climatological annual cycle, resulting in the left side of Eq. (4) tending toward zero. We first obtained the climatological monthly maps of the dissolved oxygen fluxes due to the four physical processes over one year by gridding local estimates of the fluxes from individual profiles or using gridded products (Methods “Calculation of physical oxygen fluxes” for details), and then we obtained the monthly map of the net annual biological oxygen production as the residual.

In this study, we defined the lower boundary of the vertical integration of the dissolved oxygen budget (depth *H*) as the deeper of the annual maximum mixed layer depth (MLD) or the annual maximum euphotic layer depth (*Z*_{eu}) (Fig. 1). We used the depth-sorted 95th percentiles of Argo temperature/salinity-based MLD⁷³ and satellite-derived *Z*_{eu}⁷⁴. By using this definition of *H*, which is always deeper than MLD and remains constant over time, we avoided the direct calculation of considerably large vertical diffusion fluxes within the mixed layer and the entrainment fluxes due to time-varying MLDs, which could be substantial sources of error. In addition, choosing *H* deeper than (or equal to) the annual maximum *Z*_{eu} throughout the year allows us to capture almost all of the photosynthetic production near the sea surface, including productions that occurs below the

summer shallow MLD but above Z_{eu} . However, note that in regions where winter convection reaches several times deeper than Z_{eu} , the value obtained for net biological oxygen production (hence also $ANCP_H$) may strongly reflect the respiration below Z_{eu} .

Calculation of physical oxygen fluxes

We used a parameterization for estimating air–sea oxygen exchange based on numerical simulation⁷⁵ and optimized using field measurements⁷⁶. The air–sea oxygen exchange (F_{A-S}) is represented as the sum of the diffusive flux (F_s) and the bubble fluxes (F_p and F_c):

$$F_{A-S} = (F_s + \beta F_p + \beta F_c) \times (1 - f_{ice}),$$

$$F_s = k_s \left(\frac{P_{slp}}{P_{atm}} [O_2]_s^{sat} - [O_2]_s \right)$$

$$F_p = k_p \left((1 + \Delta P) \frac{P_{slp}}{P_{atm}} [O_2]_s^{sat} - [O_2]_s \right),$$

$$F_c = k_c \chi_{atm}^{O_2}, \quad (5)$$

where $\beta, f_{ice}, P_{slp}, P_{atm}$, and $\chi_{atm}^{O_2}$ indicate a tuning parameter optimized by field measurements⁷⁶ ($\beta = 0.37$), the sea ice fraction, the sea level pressure, one standard atmospheric pressure, and atmospheric mole fraction of oxygen, respectively. k_s, k_p , and k_c are mass transfer coefficients for each of the fluxes that govern the air–sea oxygen exchange velocity and are given as a function of wind speed.

We used daily wind speed data from satellite observations (third generation of the Japanese Ocean Flux Data Sets with Use of Remote-Sensing Observation⁷⁷, J-OFURO3), atmospheric reanalysis products (Japanese 55-year Reanalysis⁷⁸, JRA55; Modern-Era Retrospective Analysis for Research and Applications version 2⁷⁹, MERRA2; and ECMWF Reanalysis version 5⁸⁰, ERA5), and their combination (Cross-Calibrated Multi-Platform version 2.0⁸¹, CCMPv2), daily sea level pressure data from ERA5, and satellite-derived daily sea ice concentration data⁸² from the National Snow and Ice Data Center. Wind speeds, sea level pressure, and sea ice concentrations were spatially interpolated to get values at the locations of individual ship/float profiles. Sea surface oxygen saturation concentrations⁸³ ($[O_2]_s^{sat}$) were calculated from sea surface temperature and salinity obtained from profiles, using a skin temperature correction following a previous study⁵². The three components of air–sea oxygen exchange were estimated from the interpolated wind speeds, sea level pressure and sea ice concentrations, and sea surface oxygen concentrations ($[O_2]_s$) from individual profiles (see also Supplementary Note 2 for further details).

The vertical diffusion term (F_{vDIFF} , the second term on the right side of Eq. [4]) was calculated as the product of the vertical gradient of dissolved oxygen and the vertical eddy diffusion coefficient at depth H . The vertical eddy diffusion coefficients at depth H are estimated on the basis of the upper ocean turbulence observations⁸⁴ by assuming a profile that decreases exponentially with an e -folding scale of 20 m as it goes deeper from the diffusion coefficient at the base of the mixed layer (κ_v^{mb}), and approaches the background diffusion coefficient (κ_v^{bg}):

$$\kappa_v(t, x, y, z = -H) = \kappa_v^{bg} + (\kappa_v^{mb} - \kappa_v^{bg}) e^{-\frac{(H-MLD(t))}{20m}}. \quad (6)$$

We used monthly vertical diffusion coefficients at the base of the mixed layer⁸⁵ obtained from the mixed layer temperature/salinity budget using time-series observations at the ocean stations located in the NH, which are also validated by observational estimates based on budgets using other tracers^{86,87}. The monthly vertical diffusion coefficients shifted by six months were used for the SH profiles, and the annual means were used for profiles in the tropics (20°S–20°N). For the background vertical diffusion coefficient, we mainly used two global observational products based on an inverse

estimation from the salinity distribution on isopycnal surfaces⁸⁸ and a fine-structure parameterization⁸⁹, in addition to a product based on energy-constrained parameterization of tidal mixing⁹⁰. κ_v^{bg} was computed using the values from the products at depths sufficiently far from depth H (averaged over the depth from $H + 100$ m to $H + 750$ m, Supplementary Fig. 2). We calculated the vertical dissolved oxygen gradient at depths H and MLD from individual profiles that were vertically interpolated at 2-m intervals by using the Akima interpolation. With the estimated vertical diffusive coefficient at depth H from Eq. (6), we computed the oxygen fluxes due to vertical diffusion for individual profiles.

The spatially non-uniformly distributed profile values of vertically integrated oxygen concentration (O_{2int}) itself, the air–sea oxygen exchange (F_{A-S}), and vertical diffusion (F_{vDIFF}) were mapped monthly to a 1° (latitude) × 1° (longitude) grid. First, we averaged the profile values in 1° (latitude) × 1° (longitude) bins, excluding values that are outside the range of two standard deviations of profile values within the bins (referred to as a grid value). Next, we conducted a Gaussian distance-weighted averaging for each grid point by searching for grid values over an elliptical shaped area with a latitude:longitude distance ratio of 1:2. The size of the ellipse (i.e., the influence radius) was increased at each grid point until there were at least seven grid values inside the ellipse. To avoid spatially excessive mapping due to the scarcity of original profile values, we also mapped the sea surface temperature obtained from the same profiles using the same mapping procedures. If the resulting mapped sea surface temperatures differed from the independent climatology of a satellite-derived sea surface temperature product (NOAA Extended Reconstructed SST version 5⁹¹) by more than double the interannual standard deviation, the mapped values were masked as missing in the discussions of local dissolved oxygen balance.

We calculated the advection term (F_{ADV} , the fourth term on the right side of Eq. [4]) using two dissolved oxygen gridded products (WOA 2018 and GOBAI- O_2) along with velocity estimated from observational temperature/salinity fields (the Roemmich-Gilson Argo Climatology⁹²) and surface wind fields (J-OFURO3, JRA55, ERA5, MERRA2), and velocities from ocean reanalysis products (Estimating the Circulation and Climate of the Ocean version 4 release 4⁹³, ECCOV4r4; and Estimated State of Global Ocean for Climate Research version 05a⁹⁴, ESTOC). The observation-based horizontal velocity was represented as the sum of the geostrophic current velocity and the Ekman current velocity. Except for the equatorial region (5°S–5°N), the geostrophic component was estimated from three-dimensional temperature and salinity fields⁹² with the assumption that the reference level is at a depth of 1975 dbar, and the Ekman component was obtained from the sea surface wind stress fields^{77–80} through non-stratified classical Ekman theory. The vertical velocities were then derived by integrating the continuity equation for an incompressible fluid using estimated horizontal velocities with the boundary condition of no vertical motion at the surface. The Gent-McWilliams ocean bolus velocity from the ECCOV4r4 was used as the bolus component of the velocity field.

We used observational gridded products for the horizontal diffusion coefficients based on an inverse estimation⁸⁸ and a mixing-length parameterization⁹⁵ using Argo salinity on isopycnal surfaces to calculate the horizontal diffusion of oxygen (F_{hDIFF} , the third term on the right side of Eq. [4]). The horizontal diffusion fluxes were calculated at a horizontal resolution of 1° (latitude) × 1° (longitude) from horizontal diffusion coefficient and gridded dissolved oxygen products (WOA 2018 and GOBAI- O_2). For purposes of visualization, the calculated horizontal diffusion and advection terms were spatially smoothed to align their spatial scales with those of mapped air–sea exchange and vertical diffusion terms (e.g., in Fig. 2c, d). This spatial smoothing does not impact the calculation of the globally integrated values summarized in Fig. 3.

The globally integrated values for physical oxygen fluxes summarized in Fig. 3 were computed with consideration for the data grids missing due to an insufficient number of profiles, or regions not covered by data products. After deriving the mean values for fluxes from values at available grid points which covers ~77% area of the global ocean, we obtained globally integrated fluxes by multiplying the mean values by the area of the global ocean.

Uncertainty estimation

In several previous studies on estimation of local ANCP through dissolved oxygen budgets^{30,32} and the syntheses of these⁹⁶, the measurement error of dissolved oxygen concentration itself has been highlighted as a major source of uncertainty. In profiles from the BGC-Argo floats, which are the primary data source for this study, potential errors of 1% or 3 $\mu\text{mol O}_2 \text{ kg}^{-1}$ have been reported, even after applying the QC procedures⁹⁷. Our comparison of float observation data, which has been QCed uniformly through the millions of profiles following a common protocol, with shipboard observations (GLODAP), which has been extensively processed to ensure the accuracy and consistency of the data, also indicates the differences of ~1% in the surface oxygen concentrations (Supplementary Fig. 5). In the calculation of the air–sea oxygen exchange, an error of 0.5–1% in surface dissolved oxygen concentration (typically around 300 $\mu\text{mol O}_2 \text{ kg}^{-1}$) could translate to an error in the flux estimate of 0.5–1 $\text{mol O}_2 \text{ m}^{-2} \text{ year}^{-1}$ (i.e., equivalent to an ANCP of 0.35–0.70 $\text{mol C m}^{-2} \text{ year}^{-1}$).

In the estimation of physical oxygen fluxes derived from individual profiles (air–sea exchange and vertical diffusion), a Monte Carlo approach was employed to quantify associated uncertainties. In order to calculate the air–sea flux, a randomly selected wind value was taken from a normal distribution with an average value of five spatially interpolated daily wind products and a standard deviation of five values. A surface oxygen concentration was also randomly taken from a normal distribution with the observed surface oxygen as the mean and the 1% error of the mean as the standard deviation. In the calculation of the vertical diffusion flux, a background diffusivity was randomly taken from the two independent products, and for the diffusivity at the base of the mixed layer a 100% error of the monthly diffusion coefficient was assumed, as reported by the previous study⁸⁵. For each profile, these flux calculations were repeated 1,500 times using randomly selected values. The mean of these iterations was taken as the flux value, and its standard deviation was employed as a measure of uncertainty. Flux values and their errors, obtained from 1,500 repeated calculations across ~600,000 profiles, were spatially mapped to a 1° (longitude) × 1° (latitude) grid using the mapping method described above. The errors associated with the integrated fluxes (e.g. Fig. 3) are reported as the simple summation of the mapped errors.

In the estimation of physical oxygen fluxes with use of the gridded oxygen products (advection and horizontal diffusion), we assessed the uncertainties from differences in the products and methodologies (referred to as “methodological uncertainty”). We estimated the methodological uncertainties by using multiple plausible parameters, data products, and calculation methods to calculate each physical oxygen flux, and then by computing standard deviations of the results obtained from the combinations of these. For the advection, advection (bolus), and horizontal diffusion components, the numbers of combinations are 6 (2), and 4, respectively (Supplementary Table 2).

The uncertainties estimated for each physical oxygen flux propagate into the estimate of net biological oxygen production (Eq. [2]) as the square root of the sum of variances. The uncertainty in the photosynthetic stoichiometry ($\Delta\text{O}_2/\Delta\text{C} = 1.45 \pm 0.03$)³³ was also taken into account when converting net biological oxygen production into ANCP.

Data availability

Dissolved oxygen profiles used in this study are available through the World Ocean Database 2018 (<https://www.ncei.noaa.gov/products/world-ocean-database>, accessed June 2022), the Argo Global Data Center (<https://usgodae.org/ftp/outgoing/argo/>, accessed September 2022, <https://doi.org/10.17882/42182#95967>), and the Global Ocean Data Analysis Project (<https://glodap.info/index.php/merged-and-adjusted-data-product-v2-2022/>, accessed December 2022). The two global oxygen gridded products are the World Ocean Atlas 2018; Dissolved Oxygen (downloaded from <https://www.ncei.noaa.gov/access/world-ocean-atlas-2018/bin/woa18oxnu.pl>, accessed June 2022) and Gridded Ocean Biogeochemistry from Artificial Intelligence; Oxygen (downloaded from <https://www.pmel>

[noaa.gov/gobai/](https://www.pmel.noaa.gov/gobai/), accessed June 2022, <https://doi.org/10.25921/z72m-yz67>). The monthly MLD product is available from <https://www.pmel.noaa.gov/gosml/> (accessed September 2022). The satellite euphotic layer depth product was downloaded from <https://oceancolor.gsfc.nasa.gov/> (accessed August 2022). The five wind products used in this study are available from https://search.diasjp.net/en/dataset/JOFURO3_V1_1 (the third generation of the Japanese Ocean Flux Data Sets with Use of Remote-Sensing Observation, accessed August 2022), <http://database.rish.kyoto-u.ac.jp/arch/jra55/> (the Japanese 55-year Reanalysis, accessed January 2023), <https://goldsmr4.gesdisc.eosdis.nasa.gov/data/MERRA2/> (the Modern-Era Retrospective Analysis for Research and Applications version 2, accessed December 2022), <https://cds.climate.copernicus.eu/cdsapp#!/dataset/reanalysis-era5-single-levels-preliminary-back-extension> (the ECMWF Reanalysis version 5, accessed December 2022), and <https://www.remss.com/measurements/ccmp/> (the Cross-Calibrated Multi-Platform version 2.0, accessed January 2023). The sea level pressure and skin layer temperature from ERA5 are also available from the above source (accessed March 2024). The satellite-derived sea ice concentration data were provided by the National Snow and Ice Data Center (<https://nsidc.org/data/nsidc-0051/versions/2>, accessed December 2022). The vertical diffusion coefficient data is available from <https://doi.org/10.17882/73082> (accessed December 2022). The satellite sea surface temperature product used for validation of our mapping is available from <https://psl.noaa.gov/data/gridded/data.noaa.ersst.v5.html> (accessed August 2022). The three-dimensional temperature/salinity climatology was downloaded from https://sio-argo.ucsd.edu/RG_Climatology.html (accessed August 2022). The ocean velocity fields from two ocean state estimates are available from https://podaac.jpl.nasa.gov/dataset/ECCO_L4 Ancillary Data V4R4 (accessed January 2023) and <https://www.godac.jamstec.go.jp/estoc/jdescription/05a.html> (accessed January 2023, <https://doi.org/10.17596/0000106>). The bolus component was obtained from http://apdrc.soest.hawaii.edu/datadoc/ecco_v4r4.php (accessed May 2023). The horizontal diffusion coefficient product is available from <https://hdl.handle.net/1912/10220> (accessed February 2023). The three products of satellite-derived NPP data (VGPM, CbPM, and CAFE) used for computing export ratios are available from <https://sites.science.oregonstate.edu/ocean.productivity/> (accessed November 2022). The observation-based global monthly gridded air–sea CO₂ flux products are available from <https://zenodo.org/records/7990823> (accessed June 2024). Source data for figures is available in <https://doi.org/10.5281/zenodo.13148073>.

Code availability

Codes to reproduce all figures in this paper are available in <https://doi.org/10.5281/zenodo.13148073>.

Received: 5 October 2023; Accepted: 6 November 2024;

Published online: 16 December 2024

References

- DeVries, T. The Ocean Carbon Cycle. *Annu. Rev. Environ. Resour.* **47**, 317–341 (2022).
- Revelle, R. & Suess, H. E. Carbon Dioxide Exchange Between Atmosphere and Ocean and the Question of an Increase of Atmospheric CO₂ during the Past Decades. *Tellus* **9**, 18–27 (1957).
- Broecker, W. S. Glacial to interglacial changes in ocean chemistry. *Prog. Oceanogr.* **11**, 151–197 (1982).
- Carlson, C. A., Ducklow, H. W. & Michaels, A. F. Annual flux of dissolved organic carbon from the euphotic zone in the northwestern Sargasso Sea. *Nature* **371**, 405–408 (1994).
- Hansell, D., Carlson, C., Repeta, D. & Schlitzer, R. Dissolved Organic Matter in the Ocean: A Controversy Stimulates New Insights. *Oceanogr.* **22**, 202–211 (2009).
- Omand, M. M. et al. Eddy-driven subduction exports particulate organic carbon from the spring bloom. *Science* **348**, 222–225 (2015).

7. Stukel, M. R. et al. Mesoscale ocean fronts enhance carbon export due to gravitational sinking and subduction. *Proc. Natl Acad. Sci.* **114**, 1252–1257 (2017).
8. Llorc, J. et al. Evaluating Southern Ocean Carbon Eddy-Pump From Biogeochemical-Argo Floats. *J. Geophys. Res. Oceans* **123**, 971–984 (2018).
9. Resplandy, L., Lévy, M. & McGillicuddy, D. J. Jr. Effects of Eddy-Driven Subduction on Ocean Biological Carbon Pump. *Glob. Biogeochemical Cycles* **33**, 1071–1084 (2019).
10. Jónasdóttir, S. H., Visser, A. W., Richardson, K. & Heath, M. R. Seasonal copepod lipid pump promotes carbon sequestration in the deep North Atlantic. *Proc. Natl Acad. Sci.* **112**, 12122–12126 (2015).
11. Boyd, P. W., Claustre, H., Levy, M., Siegel, D. A. & Weber, T. Multifaceted particle pumps drive carbon sequestration in the ocean. *Nature* **568**, 327–335 (2019).
12. Emerson, S. Annual net community production and the biological carbon flux in the ocean. *Glob. Biogeochemical Cycles* **28**, 14–28 (2014).
13. Siegel, D. A., DeVries, T., Cetinić, I. & Bisson, K. M. Quantifying the Ocean's Biological Pump and Its Carbon Cycle Impacts on Global Scales. *Annu. Rev. Mar. Sci.* **15**, 329–356 (2023).
14. Quay, P., Emerson, S., & Palevsky, H. Regional Pattern of the Ocean's Biological Pump Based on Geochemical Observations. *Geophys. Res. Lett.* **47**, e2020GL088098 (2020).
15. Laws, E. A., D'Sa, E. & Naik, P. Simple equations to estimate ratios of new or export production to total production from satellite-derived estimates of sea surface temperature and primary production. *Limnol. Oceanogr.: Methods* **9**, 593–601 (2011).
16. Westberry, T. K., Williams, P. J. le B. & Behrenfeld, M. J. Global net community production and the putative net heterotrophy of the oligotrophic oceans. *Global Biogeochemical Cycles* **26**, GB4019 (2012).
17. Lee, K. Global net community production estimated from the annual cycle of surface water total dissolved inorganic carbon. *Limnol. Oceanogr.* **46**, 1287–1297 (2001).
18. Keppler, L., Landschützer, P., Gruber, N., Lauvset, S. K. & Stemmler, I. Seasonal Carbon Dynamics in the Near-Global Ocean. *Global Biogeochem. Cycles* **34**, e2020GB006571 (2020).
19. Henson, S. A. et al. A reduced estimate of the strength of the ocean's biological carbon pump. *Geophys. Res. Lett.* **38**, L04606 (2011).
20. Dunne, J. P., Armstrong, R. A., Gnanadesikan, A. & Sarmiento, J. L. Empirical and mechanistic models for the particle export ratio. *Global Biogeochemical Cycles* **19**, GB4026 (2005).
21. Siegel, D. A. et al. Global assessment of ocean carbon export by combining satellite observations and food-web models. *Glob. Biogeochem. Cycles* **28**, 181–196 (2014).
22. DeVries, T. & Weber, T. The export and fate of organic matter in the ocean: New constraints from combining satellite and oceanographic tracer observations. *Glob. Biogeochemical Cycles* **31**, 535–555 (2017).
23. Nowicki, M., DeVries, T. & Siegel, D. A. Quantifying the Carbon Export and Sequestration Pathways of the Ocean's Biological Carbon Pump. *Glob. Biogeochemical Cycles* **36**, e2021GB007083 (2022).
24. Friedlingstein, P. et al. Global Carbon Budget 2023. *Earth Syst. Sci. Data* **15**, 5301–5369 (2023).
25. Henson, S. A. et al. Uncertain response of ocean biological carbon export in a changing world. *Nat. Geosci.* <https://doi.org/10.1038/s41561-022-00927-0> (2022).
26. Bushinsky, S. M., Emerson, S. R., Riser, S. C. & Swift, D. D. Accurate oxygen measurements on modified Argo floats using in situ air calibrations. *Limnol. Oceanogr.: Methods* **14**, 491–505 (2016).
27. Emerson, S. & Yang, B. The Ocean's Biological Pump: In Situ Oxygen Measurements in the Subtropical Oceans. *Geophys. Res. Lett.* **49**, e2022GL099834 (2022).
28. Biogeochemical-Argo Planning Group. The scientific rationale, design and implementation plan for a Biogeochemical-Argo float array. <https://doi.org/10.13155/46601> (2016).
29. Redfield, A. C., Ketchum, B. H. & Richards, F. A. The influence of organisms on the composition of sea water. In *The Sea* vol. 2 26–77 (Interscience, 1963).
30. Bushinsky, S. M. & Emerson, S. Marine biological production from in situ oxygen measurements on a profiling float in the subarctic Pacific Ocean. *Glob. Biogeochem. Cycles* **29**, 2050–2060 (2015).
31. Plant, J. N. et al. Net community production at Ocean Station Papa observed with nitrate and oxygen sensors on profiling floats. *Glob. Biogeochem. Cycles* **30**, 859–879 (2016).
32. Yang, B., Emerson, S. R. & Bushinsky, S. M. Annual net community production in the subtropical Pacific Ocean from in situ oxygen measurements on profiling floats. *Glob. Biogeochemical Cycles* **31**, 728–744 (2017).
33. Hedges, J. I. et al. The biochemical and elemental compositions of marine plankton: A NMR perspective. *Mar. Chem.* **78**, 47–63 (2002).
34. Palevsky, H. I. & Quay, P. D. Influence of biological carbon export on ocean carbon uptake over the annual cycle across the North Pacific Ocean: Influences on North Pacific Ocean CO₂ Uptake. *Glob. Biogeochem. Cycles* **31**, 81–95 (2017).
35. Schmidtko, S., Stramma, L. & Visbeck, M. Decline in global oceanic oxygen content during the past five decades. *Nature* **542**, 335–339 (2017).
36. Helm, K. P., Bindoff, N. L. & Church, J. A. Observed decreases in oxygen content of the global ocean. *Geophys. Res. Lett.* **38**, 23602 (2011).
37. Ito, T., Minobe, S., Long, M. C. & Deutsch, C. Upper ocean O₂ trends: 1958–2015. *Geophys. Res. Lett.* **44**, 4214–4223 (2017).
38. Plattner, G.-K., Joos, F. & Stocker, T. F. Revision of the global carbon budget due to changing air-sea oxygen fluxes. *Glob. Biogeochemical Cycles* **16**, 43-1–43-12 (2002).
39. Manning, A. C. & Keeling, R. F. *Glob. Ocean. land Biot. carbon sinks Scripps Atmos. Oxyg. flask Sampl. Netw.* **58**, 95 (2006).
40. Keeling, R. F. & Manning, A. C. 5.15 - Studies of Recent Changes in Atmospheric O₂ Content. in *Treatise on Geochemistry (Second Edition)* (eds. Holland, H. D. & Turekian, K. K.) 385–404 (Elsevier, Oxford, 2014). <https://doi.org/10.1016/B978-0-08-095975-7.00420-4>.
41. Tohjima, Y., Mukai, H., Machida, T., Hoshina, Y. & Nakaoka, S.-I. Global carbon budgets estimated from atmospheric O₂/N₂ and CO₂ observations in the western Pacific region over a 15-year period. *Atmos. Chem. Phys.* **19**, 9269–9285 (2019).
42. Li, C. et al. Estimation of Oceanic and Land Carbon Sinks Based on the Most Recent Oxygen Budget. *Earth's Future* **9**, e2021EF002124 (2021).
43. Portela, E., Kolodziejczyk, N., Vic, C. & Thierry, V. Physical Mechanisms Driving Oxygen Subduction in the Global Ocean. *Geophys. Res. Lett.* **47**, e2020GL089040 (2020).
44. Liu, L. L. & Huang, R. X. The Global Subduction/Obduction Rates: Their Interannual and Decadal Variability. *J. Clim.* **25**, 1096–1115 (2012).
45. Quay, P. Organic Matter Export Rates and the Pathways of Nutrient Supply in the Ocean. *Glob. Biogeochemical Cycles* **37**, e2023GB007855 (2023).
46. Rodgers, K. B. et al. Low-latitude mesopelagic nutrient recycling controls productivity and export. *Nature* **632**, 802–807 (2024).
47. Palevsky, H. I. & Doney, S. C. How Choice of Depth Horizon Influences the Estimated Spatial Patterns and Global Magnitude of Ocean Carbon Export Flux. *Geophys. Res. Lett.* **45**, 4171–4179 (2018).
48. Wang, Z., Garcia, H. E., Boyer, T. P., Reagan, J. & Cebrian, J. Controlling factors of the climatological annual cycle of the surface mixed layer oxygen content: A global view. *Front. Marine Sci.* **9**, (2022).

49. Binetti, U. et al. Net community oxygen production derived from Seaglider deployments at the Porcupine Abyssal Plain site (PAP; northeast Atlantic) in 2012–13. *Prog. Oceanogr.* **183**, 102293 (2020).
50. Johnson, K. S., Plant, J. N., Dunne, J. P., Talley, L. D. & Sarmiento, J. L. Annual nitrate drawdown observed by SOCCOM profiling floats and the relationship to annual net community production. *J. Geophys. Res. Oceans* **122**, 6668–6683 (2017).
51. Arteaga, L. A., Pahlow, M., Bushinsky, S. M. & Sarmiento, J. L. Nutrient Controls on Export Production in the Southern Ocean. *Glob. Biogeochem. Cycles* **33**, 942–956 (2019).
52. Yang, B., Emerson, S. R. & Cronin, M. F. Skin Temperature Correction for Calculations of Air–Sea Oxygen Flux and Annual Net Community Production. *Geophys. Res. Lett.* **49**, e2021GL096103 (2022).
53. Qiu, B. & Huang, R. X. Ventilation of the North Atlantic and North Pacific: subduction versus obduction. *J. Phys. Oceanogr.* **25**, 2374–2390 (1995).
54. Bushinsky, S. M. & Emerson, S. R. Biological and physical controls on the oxygen cycle in the Kuroshio Extension from an array of profiling floats. *Deep Sea Res. Part I Oceanographic Res. Pap.* **141**, 51–70 (2018).
55. Pelland, N. A., Eriksen, C. C., Emerson, S. R. & Cronin, M. F. Seaglider Surveys at Ocean Station Papa: Oxygen Kinematics and Upper-Ocean Metabolism. *J. Geophys. Res.: Oceans* **123**, 6408–6427 (2018).
56. Martz, T. R., Johnson, K. S. & Riser, S. C. Ocean metabolism observed with oxygen sensors on profiling floats in the South Pacific. *Limnol. Oceanogr.* **53**, 2094–2111 (2008).
57. Su, J., Schallenberg, C., Rohr, T., Strutton, P. G. & Phillips, H. E. New Estimates of Southern Ocean Annual Net Community Production Revealed by BGC–Argo Floats. *Geophys. Res. Lett.* **49**, e2021GL097372 (2022).
58. Behrenfeld, M. J. & Falkowski, P. G. Photosynthetic rates derived from satellite-based chlorophyll concentration. *Limnol. Oceanogr.* **42**, 1–20 (1997).
59. Westberry, T., Behrenfeld, M. J., Siegel, D. A. & Boss, E. Carbon-based primary productivity modeling with vertically resolved photoacclimation: CARBON-BASED PRODUCTION MODEL. *Glob. Biogeochem. Cycles* **22**, n/a–n/a (2008).
60. Silsbe, G. M., Behrenfeld, M. J., Halsey, K. H., Milligan, A. J. & Westberry, T. K. The CAFE model: A net production model for global ocean phytoplankton. *Glob. Biogeochemical Cycles* **30**, 1756–1777 (2016).
61. Li, Z. & Cassar, N. Satellite estimates of net community production based on O₂/Ar observations and comparison to other estimates. *Glob. Biogeochemical Cycles* **30**, 735–752 (2016).
62. Johnson, K. S. & Bif, M. B. Constraint on net primary productivity of the global ocean by Argo oxygen measurements. *Nat. Geosci.* **14**, 769–774 (2021).
63. Levy, M. et al. Physical pathways for carbon transfers between the surface mixed layer and the ocean interior. *Glob. Biogeochem. Cycles* **27**, 1001–1012 (2013).
64. Wang, W. L. et al. Biological carbon pump estimate based on multidecadal hydrographic data. *Nature* **624**, 579–585 (2023).
65. Jenkins, W. J. & Goldman, J. C. Seasonal oxygen cycling and primary production in the Sargasso Sea. *J. Mar. Res.* **43**, 465–491 (1985).
66. Emerson, S. Seasonal oxygen cycles and biological new production in surface waters of the subarctic Pacific Ocean. *J. Geophys. Res.: Oceans* **92**, 6535–6544 (1987).
67. Boyer, T. P. et al. World ocean database. *NOAA Atlas NESDIS* **87**, 2018 (2018).
68. Thierry, V. et al. *Processing Argo oxygen data at the DAC level* (Ifremer, 2022).
69. Lauvset, S. K. et al. GLODAPv2.2022: the latest version of the global interior ocean biogeochemical data product. *Earth Syst. Sci. Data* **14**, 5543–5572 (2022).
70. Thierry, V., Bittig, H. & The Argo–Bgc Team. *Argo quality control manual for dissolved oxygen concentration* (The Argo–Bgc Team, 2021).
71. Garcia, H. E. et al. *WORLD OCEAN ATLAS 2018 Volume 3: Dissolved Oxygen, Apparent Oxygen Utilization, and Dissolved Oxygen Saturation*, 83 (NOAA Atlas NESDIS, 2019).
72. Sharp, J. D. et al. GOBAL-O₂: temporally and spatially resolved fields of ocean interior dissolved oxygen over nearly 2 decades. *Earth Syst. Sci. Data* **15**, 4481–4518 (2023).
73. Johnson, G. C. & Lyman, J. M. GOSML: A Global Ocean Surface Mixed Layer Statistical Monthly Climatology: Means, Percentiles, Skewness, and Kurtosis. *JGR Oceans* **127**, e2021JC018219 (2022).
74. Lee, Z. et al. Euphotic zone depth: Its derivation and implication to ocean-color remote sensing. *J. Geophys. Res. Oceans* **112**, C03009 (2007).
75. Liang, J.-H. et al. Parameterizing bubble-mediated air–sea gas exchange and its effect on ocean ventilation. *Glob. Biogeochem. Cycles* **27**, 894–905 (2013).
76. Emerson, S., Yang, B., White, M. & Cronin, M. Air–Sea Gas Transfer: Determining Bubble Fluxes With In Situ N₂ Observations. *J. Geophys. Res. Oceans* **124**, 2716–2727 (2019).
77. Tomita, H., Hihara, T., Kako, S., Kubota, M. & Kutsuwada, K. An introduction to J-OFURO3, a third-generation Japanese ocean flux data set using remote-sensing observations. *J. Oceanogr.* **75**, 171–194 (2019).
78. Kobayashi, S. et al. The JRA-55 Reanalysis: General Specifications and Basic Characteristics. *J. Meteorological Soc. Jpn.* **93**, 5–48 (2015).
79. Gelaro, R. et al. The Modern-Era Retrospective Analysis for Research and Applications, Version 2 (MERRA-2). *J. Clim.* **30**, 5419–5454 (2017).
80. Hersbach, H. et al. The ERA5 global reanalysis. *Q. J. R. Meteorological Soc.* **146**, 1999–2049 (2020).
81. Mears, C. A. et al. A Near-Real-Time Version of the Cross-Calibrated Multiplatform (CCMP) Ocean Surface Wind Velocity Data Set. *JGR Oceans* **124**, 6997–7010 (2019).
82. DiGirolamo, N. E., Parkinson, C. L., Cavalieri, D. J., Gloersen, P. & Zwally, H. J. Sea Ice Concentrations from Nimbus-7 SMMR and DMSP SSM/I–SSMIS Passive Microwave Data. NASA National Snow and Ice Data Center Distributed Active Archive Center, <https://doi.org/10.5067/MPYG15WAA4WX> (2022).
83. Garcia, H. E. & Gordon, L. I. Oxygen solubility in seawater: Better fitting equations. *Limnol. Oceanogr.* **37**, 1307–1312 (1992).
84. Sun, O. M., Jayne, S. R., Polzin, K. L., Rahter, B. A. & St. Laurent, L. C. Scaling Turbulent Dissipation in the Transition Layer. *J. Phys. Oceanogr.* **43**, 2475–2489 (2013).
85. Cronin, M. F., Pelland, N. A., Emerson, S. R. & Crawford, W. R. Estimating diffusivity from the mixed layer heat and salt balances in the North Pacific. *J. Geophys. Res. Oceans* **120**, 7346–7362 (2015).
86. Sukigara, C. et al. Biogeochemical evidence of large diapycnal diffusivity associated with the subtropical mode water of the North Pacific. *J. Oceanogr.* **67**, 77–85 (2011).
87. Qiu, B. et al. Observations of the Subtropical Mode Water Evolution from the Kuroshio Extension System Study. *J. Phys. Oceanogr.* **36**, 457–473 (2006).
88. Kouketsu, S. Inverse estimation of diffusivity coefficients from salinity distributions on isopycnal surfaces using Argo float array data. *J. Oceanogr.* **77**, 615–630 (2021).
89. Whalen, C. B., MacKinnon, J. A. & Talley, L. D. Large-scale impacts of the mesoscale environment on mixing from wind-driven internal waves. *Nat. Geosci.* **11**, 842–847 (2018).
90. de Lavergne, C. et al. A Parameterization of Local and Remote Tidal Mixing. *J. Adv. Model. Earth Syst.* **12**, e2020MS002065 (2020).

91. Huang, B. et al. Extended Reconstructed Sea Surface Temperature, Version 5 (ERSSTv5): Upgrades, Validations, and Intercomparisons. *J. Clim.* **30**, 8179–8205 (2017).
92. Roemmich, D. & Gilson, J. The 2004–2008 mean and annual cycle of temperature, salinity, and steric height in the global ocean from the Argo Program. *Prog. Oceanogr.* **82**, 81–100 (2009).
93. Forget, G. et al. ECCO version 4: an integrated framework for non-linear inverse modeling and global ocean state estimation. *Geoscientific Model Dev.* **8**, 3071–3104 (2015).
94. Osafune, S., Kouketsu, S., Doi, T., Sugiura, N. & Masuda, S. A global ocean state estimation using tidally induced vertical-mixing schemes. *Ocean Model.* **179**, 102111 (2022).
95. Cole, S. T., Wortham, C., Kunze, E. & Owens, W. B. Eddy stirring and horizontal diffusivity from Argo float observations: Geographic and depth variability. *Geophys. Res. Lett.* **42**, 3989–3997 (2015).
96. Izett, R. W., Fennel, K., Stoer, A. C. & Nicholson, D. P. Reviews and syntheses: expanding the global coverage of gross primary production and net community production measurements using Biogeochemical-Argo floats. *Biogeosciences* **21**, 13–47 (2024).
97. Maurer, T. L., Plant, J. N. & Johnson, K. S. Delayed-Mode Quality Control of Oxygen, Nitrate, and pH Data on SOCCOM Biogeochemical Profiling Floats. *Front. Mar. Sci.* **8**, 683207 (2021).
98. Müller, J. D. RECCAP2-ocean data collection. *Zenodo*, <https://doi.org/10.5281/zenodo.7990823> (2023).

Acknowledgements

This study owes much to the incalculable efforts of principal investigators, researchers, and captains and crews, who were responsible for acquiring shipboard data, deploying floats for profiling data, and managing the databases used for this study. The authors express their sincere gratitude to them. R.Y. thanks Dr. Katsuya Toyama, Dr. Sayaka Yasunaka, and the members of the Global Ocean Observation Research Center at JAMSTEC, for valuable and useful comments and discussions. R.Y. was supported by MEXT/JSPS KAKENHI Grant Number JP24H02221. S.K. was supported by MEXT/JSPS KAKENHI Grant Number JP22H05207. The data from BGC-Argo floats were collected and made freely available by the International Argo Program (<https://argo.ucsd.edu>) and the national programs that contribute to it (<https://www.ocean-ops.org>). The Argo Program is part of the Global Ocean Observing System. The authors acknowledge Dr. Caitlin B. Whalen and Dr. Meghan F. Cronin for providing the vertical diffusion coefficient data and Dr. Robert W. Izett for providing a comprehensive list of references for studies on NCP estimation at OSP.

Author contributions

R.Y. conceptualized the scientific framing of this study, conducted all of the analyses, and wrote the initial draft of the manuscript. R.Y., K. S., N.K., and M.I. contributed to development of the analytical methods and interpretation of the results, and contributed to writing the final draft of the manuscript.

Competing interests

The authors declare no competing interests.

Additional information

Supplementary information The online version contains supplementary material available at <https://doi.org/10.1038/s43247-024-01886-7>.

Correspondence and requests for materials should be addressed to Ryohei Yamaguchi.

Peer review information *Communications Earth & Environment* thanks Seth Bushinsky, Paul Quay and the other, anonymous, reviewer(s) for their contribution to the peer review of this work. Primary Handling Editors: Michael Stukel, Joe Aslin, Clare Davis, Heike Langenberg. [A peer review file is available.]

Reprints and permissions information is available at <http://www.nature.com/reprints>

Publisher's note Springer Nature remains neutral with regard to jurisdictional claims in published maps and institutional affiliations.

Open Access This article is licensed under a Creative Commons Attribution-NonCommercial-NoDerivatives 4.0 International License, which permits any non-commercial use, sharing, distribution and reproduction in any medium or format, as long as you give appropriate credit to the original author(s) and the source, provide a link to the Creative Commons licence, and indicate if you modified the licensed material. You do not have permission under this licence to share adapted material derived from this article or parts of it. The images or other third party material in this article are included in the article's Creative Commons licence, unless indicated otherwise in a credit line to the material. If material is not included in the article's Creative Commons licence and your intended use is not permitted by statutory regulation or exceeds the permitted use, you will need to obtain permission directly from the copyright holder. To view a copy of this licence, visit <http://creativecommons.org/licenses/by-nc-nd/4.0/>.

© The Author(s) 2024